Formic Acid Oxidation

DOI: 10.1002/anie.201408399

Size-Controlled Synthesis of Platinum–Copper Hierarchical Trigonal Bipyramid Nanoframes**

*Sheng Chen, Hongyang Su, Youcheng Wang, Wenlong Wu, and Jie Zeng**

Abstract: *Mastery over the structure of materials at nanoscale can effectively tailor and control their catalytic properties, enabling enhancement in both activity and durability. We report a size-controlled synthesis of novel Pt–Cu hierarchical trigonal bipyramid nanoframes (HTBNFs). The obtained nanocrystals looked like a trigonal bipyramid on the whole, composed of similar ordered frame structural units. By varying the amount of KI involved in the reaction, HTBNFs with variable sizes from 110 to 250 nm could be obtained. In addition, the structure of HTBNFs could be preserved only in a limited range of the Pt/Cu feeding ratio. Relative to the commercial Pt/C, these Pt–Cu HTBNFs with different Pt/Cu ratio exhibited enhanced electrocatalytic activity toward formic acid oxidation reaction as much as 5.5 times in specific activity and 2.1 times in mass activity. The excellent electrocatalytic activity and better durability are due to the unique structure of HTBNFs and probably synergetic effects between Pt and Cu.*

Platinum nanocrystals have been extensively studied because of their unique catalytic properties in various significant applications.[1] However, considering the limited resource and rising cost of Pt, there is an urgent need to find the substitute for pure Pt catalysts.[2–4] By combining less expensive transition metals, such as Cu, the formation of an alloy will not only reduce the consumption of Pt, but also enhance the overall performance due to possible synergetic effects.[5,6] Besides the composition, it is well established that the catalytic properties of metal nanocrystals are also strongly correlated with their structure.[3d,4a,7] In particular, metal nanoframes with only ridges and no side faces have attained extensive attention in catalysis and electrocatalysis.[8] The nanoframes with completely open and ultrathin structure have both high surface-to-volume ratios and large surface areas, which endows them with a high degree of dispersity (defined as the percentage of active atoms exposed at the surface of catalysts) and an improved atomic utilization coefficient as catalysts.[5b,8] In addition, the surface permeability of nanoframes will promote the possibility to interact with atoms, ions, and molecules not only at surfaces, but throughout the bulk of the nanocrystals. In other words, it can increase molecular accessibility and accelerate mass diffusion during the reaction to some extent.[6c,8e] Recently, Yang and co-workers have demonstrated the synthesis of hollow Pt_3Ni nanoframes with surfaces that have three-dimensional (3D) molecular accessibility. These catalysts exhibited over 36 and 22-fold enhancement in mass and specific activities, respectively, for the oxygen reduction reaction (ORR) in comparison to state-of-the-art Pt/C catalysts.[8e] As a special case of frame structure, the hierarchical nanoframes exhibit most of the advantages of frame structures. Besides, differently from the typical nanoframes, there are interlinked branches as bridges to connect each frame unit in the hierarchical frames.[8e] For a redox reaction, the interlinked branches of hierarchical nanoframes will develop a good 'electrical' connection between the site of oxidation and that of reduction. It will be helpful for electron transfer in the reaction and lead to a better catalytic performance.[9] For this reason, hierarchical Pt–Cu nanoframes are promising catalysts and need further exploration. To date, there are some studies on metallic hierarchical structures, but most are $>1\,\mu m$ in size.[10] Therefore, the fabrication of small-sized bimetallic hierarchical nanoframe structures, especially with sub-5 nm branches, are still in a rudimentary state of development.

Herein, we report a facile synthesis of novel ordered Pt–Cu alloy hierarchical trigonal bipyramid nanoframes (HTBNFs).[11] The obtained nanocrystals looked like a trigonal bipyramid on the whole, composed of a series of similar frame structural units with sub-5 nm branch tips. By varying the amount of KI involved in the system, differently sized Pt–Cu HTBNFs were prepared. It is found that the Pt/Cu feeding ratio was critical to the formation of Pt–Cu HTBNFs. Our catalysis study reveals that the obtained Pt–Cu HTBNFs exhibit better performance than commercial Pt/C toward the oxidation of formic acid.

In a typical synthesis of the Pt–Cu HTBNFs, an aqueous solution of $CuCl_2$, H_2PtCl_6, and KI was added into a mixture containing poly(vinyl pyrrolidone) (PVP) and ethylene glycol (EG) in a 20 mL vial. After the resulting homogeneous

[*] S. Chen,[+] H. Su,[+] Y. Wang, Prof. J. Zeng
Hefei National Laboratory for Physical Sciences at the Microscale & Collaborative Innovation Center of Suzhou Nano Science and Technology
University of Science and Technology of China
Hefei, Anhui 230026 (P. R. China)
E-mail: zengj@ustc.edu.cn
Homepage: http://zengnano.ustc.edu.cn/
W. Wu, Prof. J. Zeng
Center of Advanced Nanocatalysis (CAN-USTC) and Department of Chemical Physics
University of Science and Technology of China
Hefei, Anhui 230026 (P. R. China)
[+] These authors contributed equally to this work.

[**] This work was supported by MOST of China (2014CB932700 and 2011CB921403), the NSFC (21203173, 51371164, and J1030412), the Strategic Priority Research Program B of the CAS (XDB01020000), and the Fundamental Research Funds for the Central Universities (WK2340000050 and WK2060190025).
Supporting information for this article is available on the WWW under http://dx.doi.org/10.1002/anie.201408399.

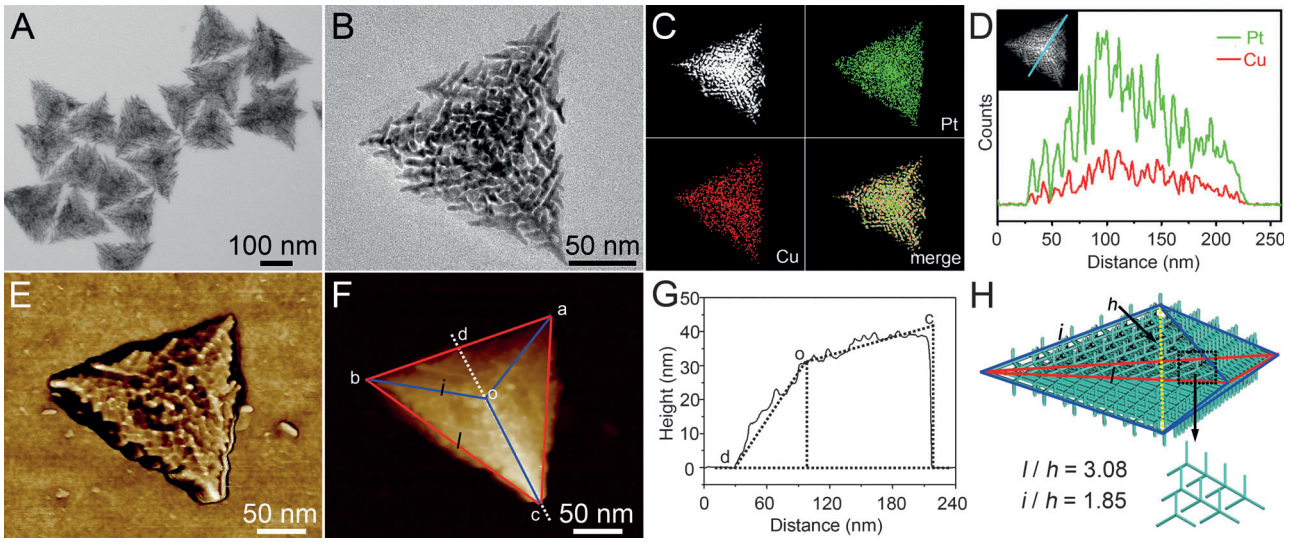

Figure 1. A,B) TEM images on a large scale (A) and of an individual (B) Pt–Cu HTBNFs. C) The corresponding HAADF-STEM image and elemental mapping images showing the distribution of Pt (green) and Cu (red). D) Line-scan profiles recorded from the individual Pt–Cu HTBNFs in Figure 1 B. E,F) The representative AFM topographic phase image (E) and height image (F) of the Pt–Cu HTBNF. G) Height profile along the short dotted line in (F). H) The schematic model of Pt–Cu HTBNFs.

mixture was transferred into an oil bath and heated at 140 °C for 90 min, the final products were collected by centrifugation, followed by washing twice with an ethanol/acetone mixture. Figure 1 A and B shows the representative transmission electron microscopy (TEM) images of Pt–Cu nanocrystals. Most of the typical products had a uniform edge length of 200 ± 20 nm. Each individual nanocrystal overall had the shape of a pyramid, but with ordered hierarchical frame units. There are three main branches in each HTBNF, with secondary, tertiary, and higher-order branches stretching outward, the sharp tips of which were less than 5 nm in diameter. The energy dispersive X-ray (EDX) spectrum (Figure S1) revealed that the nanocrystals were composed of Pt and Cu. The high-angle annular dark-field scanning transmission electron microscopy (HAADF-STEM)-EDX elemental mapping of Pt and Cu (Figure 1 C) was used to determine the distribution of Pt and Cu in the nanocrystals. The full coverage of both Pt and Cu reveals the alloy structure. The merged image of Pt and Cu (Figure 1 C) in the individual HTBNF further approves the complete overlapping of the two elements, which is also confirmed by the line scan profiles recorded from the individual HTBNF (Figure 1 D). Powder X-ray diffraction (PXRD) analysis was employed to characterize the crystallinity of the Pt–Cu HTBNFs (Figure S2). The peaks observed for the Pt–Cu HTBNFs can be indexed as a face-centered cubic (*fcc*) structure, each of which lies between those of pure *fcc* Pt (JCPDS no. 87-0646) and pure *fcc* Cu (JCPDS no. 85-1326). According to Vegard's law, it can be deduced from the XRD pattern that the ratio of Pt/Cu was approximately 3.1.[5a] In addition, Figure S3 shows the X-ray photoelectron spectroscopy (XPS) spectra of the Pt–Cu HTBNFs. The two peaks located at 74.1 eV and 70.7 eV in Figure S3A could be assigned to elemental Pt $4f_{5/2}$ and Pt $4f_{7/2}$, respectively.[12] Figure S3B demonstrates that no Cu 2p separate satellite peaks exist, indicating the absence of Cu^{2+}. Combined with the Cu LM2 (Figure S3C) auger peak at 919.4 eV, we could confirm that only metallic Cu^0 exists in the nanocrystal. The negative shift in the binding energies compared to that of pure Cu^0 (Cu $2p_{3/2}$, 932.2 eV) suggests an expansion of the atomic distance which indicates the formation of Pt–Cu alloy.[13] Comparing the ratio of Pt/Cu measured by XPS and inductively coupled plasma atomic emission spectroscopy (ICP-AES), we determined that the ratio of Pt/Cu on the surface (3.25, by XPS, Figure S3) was almost equal to that in bulk nanocrystals (3.32, by ICP-AES). All these results furnish strong evidence of the alloy structure of the HTBNFs.

Figure 1 E and F shows the representative atomic force microscopy (AFM) topographic phase image and height image of an individual HTBNF. The AFM height profile (Figure 1 G) along the short dotted line in Figure 1 F establishes that the height difference between o and d is approximately 30 nm, whereas that between c and o is merely 10 nm. The result implies that the nanocrystals may stand aslant on the silicon wafer, which suggests that the opposite side of the observed nanoframes is not just a simple plane. To further visualize the three-dimensional structure of the nanocrystals, we conducted scanning electron microscopy (SEM) characterizations of the individual Pt–Cu HTBNF in various orientations (Figure S4, A–D). It seems that the opposite side of the nanocrystals was more likely to be a structure which exhibited mirror symmetry to what we observed in TEM images. Based on the characterizations, we proposed a possible geometric model of Pt–Cu HTBNFs, as shown in Figures 1 H and S4, E–H. The model looked like a trigonal bipyramid, with the composition of frame structural units (the inset in Figure 1 H). We further calculated structural parameters of the trigonal bipyramid (Figure S5). The distance between a and b was defined as D_{ab} and the rest could be done in the same manner. Based on the top view

(Figure S5B) and the side view (Figure S5C), D_{oc}, D_{ce}, and D_{oe} were calculated to be 123.1 nm, 118.5 nm, and 33.3 nm, respectively. The edge length (D_{ab}) was 205.2 nm according to Figure 1F, so it was obtained that $l/h = 3.08$ and $i/h = 1.85$ (l, h, and i represent the edge length, the height, and the side edge length, respectively, of the trigonal bipyramid).

Figure 2A shows the representative HAADF-STEM image of a single Pt–Cu HTBNF. The inset in Figure 2A exhibits a typical selected area electron diffraction (SAED) pattern recorded from the individual nanocrystal along the

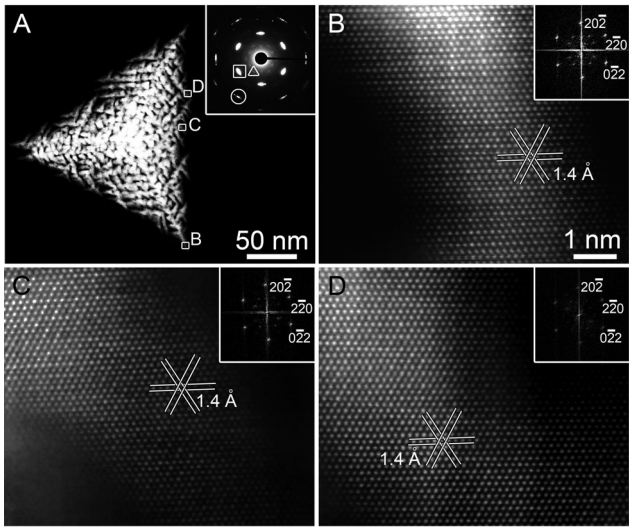

Figure 2. A) HAADF-STEM image of an individual Pt–Cu HTBNFs. The inset of (A) shows the SAED pattern taken from this particle. The spots (marked by circle, square, and triangle) could be indexed to the allowed {422} reflection, the allowed {220} reflection, and the formally forbidden 1/3{422} reflection, respectively. B–D) HAADF-HRTEM images recorded from B–D marked with white boxes in (A), respectively. Insets show corresponding FFT patterns. The scale bar in (B) also applies to (C) and (D).

⟨111⟩ direction. Three sets of spots were identified based on the *d*-spacing. The set with a spacing of 1.4 Å (square) was indexed to the {220} reflection, and the outer set with a lattice spacing of 0.8 Å (circle) originated from the {422} reflection. These two sets of reflection were both allowed for an *fcc* lattice. The other observed set with a spacing of 2.5 Å (triangle) was due to the 1/3{422} reflection, which was probably caused by the presence of a (111) planar defect (stacking fault or twin plane) in the HTBNF. Figure 2B–D shows HAADF high-resolution TEM (HRTEM) images recorded from B, C, and D marked with white boxes in Figure 2A, respectively. In these HAADF-HRTEM images, the fringes separated by 1.4 Å could be assigned to the {220} planes, as confirmed by the corresponding fast Fourier transform (FFT) patterns (insets in Figure 2B–D).

To elucidate the morphological evolution of the Pt–Cu HTBNFs, a series of TEM images were taken for the samples obtained at different reaction stages, as shown in Figure S6. At the initial stage of the reaction (8 min, Figure S6A and 10 min, Figure S6B), a mixture of monopods, bipods, and tripods were obtained. At 12 min (Figure S6C), we could preliminarily confirm the three arms of tripods as main branches in the final HTBNFs, the length of which elongated to approximately 30 nm at this stage, and that some secondary branches started to appear on the arms of the tripods. From 13 to 15 min (Figure S6, D–F), more secondary branches emerged and grew longer, meanwhile, tertiary branches also started to grow out of the secondary branches. With a reaction time of 18 min, more tertiary branches developed outward, leading to a primary feature of HTBNFs (Figure S6G). Samples obtained at 20, 30, 60, and 90 min were observed as more obvious ordered hierarchical structures, with more secondary, tertiary, and higher-order branches formed (Figure S6, H–K). The size of the samples enlarged from 70 to 200 nm (Figure S6, H–K). There was no obvious change in the morphologies of HTBNFs upon further extension of the reaction time to 120 min (Figure S6L).

To study the growth mechanism of the Pt–Cu HTBNFs, additional HAADF-STEM images of the Pt–Cu nanocrystals obtained at 10 min were taken. Figure 3B shows a monopod with 10 nm in size (1 in Figure 3A) which displays the start of single pod growth. Figure 3D shows a tripod with 20 nm in size and a secondary branch appears to grow from one of its arms (2 in Figure 3A). The HAADF-STEM images and the corresponding EDX mapping images (Figure 3C and E) exhibit the elemental distribution of Pt and Cu in the

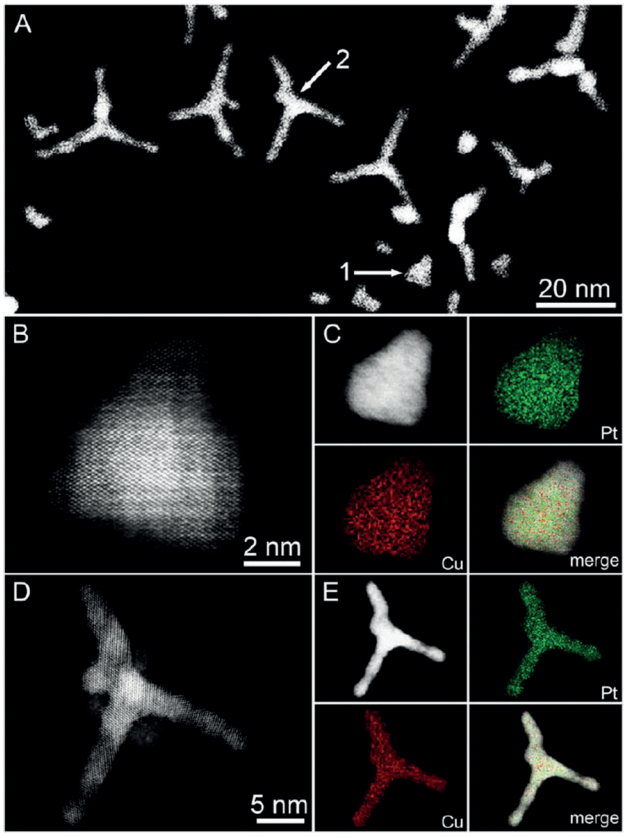

Figure 3. A) HAADF-STEM image of Pt–Cu nanocrystals obtained after 10 min reaction time. B,D) Magnified HAADF-STEM images and C,E) the corresponding elemental mapping images showing the distribution of Pt (green) and Cu (red) for Pt–Cu nanocrystals 1 and 2 marked in (A), respectively.

monopod and tripod, revealing their alloy structure. The formation of alloy structures in the initial stage of the reaction indicates the co-reduction of Pt and Cu. It is reported that the reduction potential of $PtCl_6^{2-}/Pt^0$ is far more positive than that of Cu^{2+}/Cu^0. However, I^- has stronger coordination interaction with Pt^{4+} than Cl^-, and thus I^- could replace Cl^- to form $[PtCl_{6-x}I_x]^{2-}$, resulting in a closer level of the reduction potential of $[PtI_6]^{2-}/Pt^0$ (0.40 V vs. RHE) and Cu^{2+}/Cu^0 (0.34 V vs. RHE).[14] These results reveal that the HTBNFs were formed by co-deposition of Pt^0 and Cu^0. The equilibrium can be described by the following equations:

$$PtCl_6^{2-} + x\,I^- \rightleftharpoons [PtCl_{6-x}I_x]^{2-} + (6-x)\,Cl^- \quad (1)$$

$$[PtCl_{6-x}I_x]^{2-} + 2\,e^- \rightleftharpoons Pt^0 + x\,I^- + (6-x)\,Cl^- \quad (2)$$

$$Cu^{2+} + 2\,e^- \rightleftharpoons Cu^0 \quad (3)$$

$$[PtCl_{6-x}I_x]^{2-} + Cu^{2+} + e^- \overset{\text{co-reduction}}{\rightleftharpoons} Pt^0 + Cu^0 + I^- + Cl^- \quad (4)$$

The amount of KI involved in the synthesis was shown to be the main factor influencing the size of the HTBNFs. Figure 4 shows representative TEM images of Pt–Cu HTBNFs obtained with different amounts of KI. With 30 μL of KI solution (Figure 4A), the obtained HTBNFs

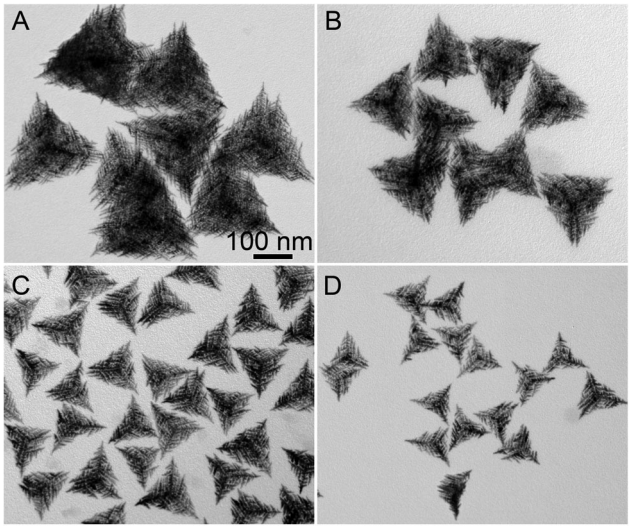

Figure 4. TEM images of Pt–Cu HTBNFs obtained through the addition of different amounts of KI aqueous solution in the synthesis while keeping the other parameters constant: A) 30 μL, B) 50 μL, C) 100 μL, and D) 150 μL. The scale bar in (A) also applies to (B–D).

were in the size of more than 250 nm. By increasing the volume of KI solution, we were able to reduce the size of the obtained HTBNFs: 200 nm for 50 μL of KI solution, 150 nm for 100 μL of KI solution, and 110 nm for 150 μL of KI solution (Figure 4B, C, and D, respectively). The SEM images shown in Figure S7 also confirm the change in the size of the products. On the basis of the ICP-AES analysis, $Pt_{3.99}Cu$, $Pt_{3.32}Cu$, $Pt_{3.19}Cu$, and $Pt_{3.07}Cu$ HTBNFs were obtained. It further implies that the formed coordination compound $[PtCl_{6-x}I_x]^{2-}$ would reduce the reduction potential of Pt^{4+}/Pt^0, and thus reduce the probability to form Pt^0, leading to the corresponding decrease in the ratio of Pt/Cu.

To gain insight into the role of Cu^{2+} in the synthesis of Pt–Cu HTBNFs, we conducted a set of experiments by changing the Pt/Cu feeding ratio while keeping the other parameters constant. In the absence of Cu^{2+} in the reaction system, the dominant products were nanoflowers 25 nm in size with randomly oriented branches (Figure S8A).[15] However, as Cu^{2+} was added and the content of Cu^{2+} increased, the shape of nanocrystals changed drastically, which indicated the critical role of Cu in the formation of HTBNFs. With only a small amount of Cu^{2+} (Pt/Cu, 7:1), a small percentage of HTBNFs ($\approx$45 nm in size) appears, together with some nanoflowers (Figure S8B). As is well established, nanocrystals with 3-fold symmetry were generated from twin structure. This result implies that the presence of Cu^{2+} leads to the change of a part of the seeds from a single-crystal to a plate-like structure with stacking faults along the vertical direction.[16] As the feeding ratio changed to 4:1, more and bigger HTBNFs were observed (Figure S8C). When the ratio of Pt/Cu was 2:1 (Figure S8D), HTBNFs similar to the typical products and a small amount of nanoflowers were obtained. One can obviously see that the products gradually changed from randomly oriented nanoflowers to ordered Pt–Cu HTBNFs from Figure S8A to Figure S8E. It indicates that more Cu^{2+} in the reaction system prompted the formation of nanocrystals with specific crystallographic direction. With a further decrease of the ratio of Pt/Cu from 1:2 to 1:7, the dominant products varied from smaller HTBNFs to a mixture of simple hierarchical structures and porous cubic nanocrystals (Figure S8, F–H). Irregular nanocrystals were obtained with pure Cu precursors involved in the reaction (Figure S8I). Based on these results, we propose a mechanism as follows. In the formation of HTBNFs, Cu^{2+} facilitated the generation of plate-like seeds at the initial stage.[16a] The underpotential deposition (UPD) of Cu would occur in this system and hinder the deposition of atoms on certain surface. The plate-like seeds grew at the corners, leading to the formation of tripods with arms along three $\langle 211 \rangle$ directions. Afterwards, the similar UPD process would work during the growth of secondary, tertiary and high-order branches along specific crystallographic directions.[16b] When the reaction was conducted in the absence of KI, only multipods (mostly tripods) were obtained (Figure S9). This result confirms that Cu promoted the formation of plate-like seeds at the early stage. It is apparent that the Pt/Cu feeding ratio is strongly related to both nucleation and growth kinetics, and thus the final morphology of products.

Motivated by the unique hierarchical frame structure of the Pt–Cu nanocrystals, we chose formic acid oxidation to examine the electrocatalytic properties of Pt–Cu HTBNFs with different Pt/Cu ratios. For comparison, commercial Pt/C was measured under the same condition. The electrochemical active surface areas (ECSAs) can be calculated by integrating the charge passing the electrode during the hydrogen adsorption/desorption process after the correction for the double layer formation.[6c] According to the cyclic voltammetry (CV) curves shown in Figure 5A, the ECSAs were

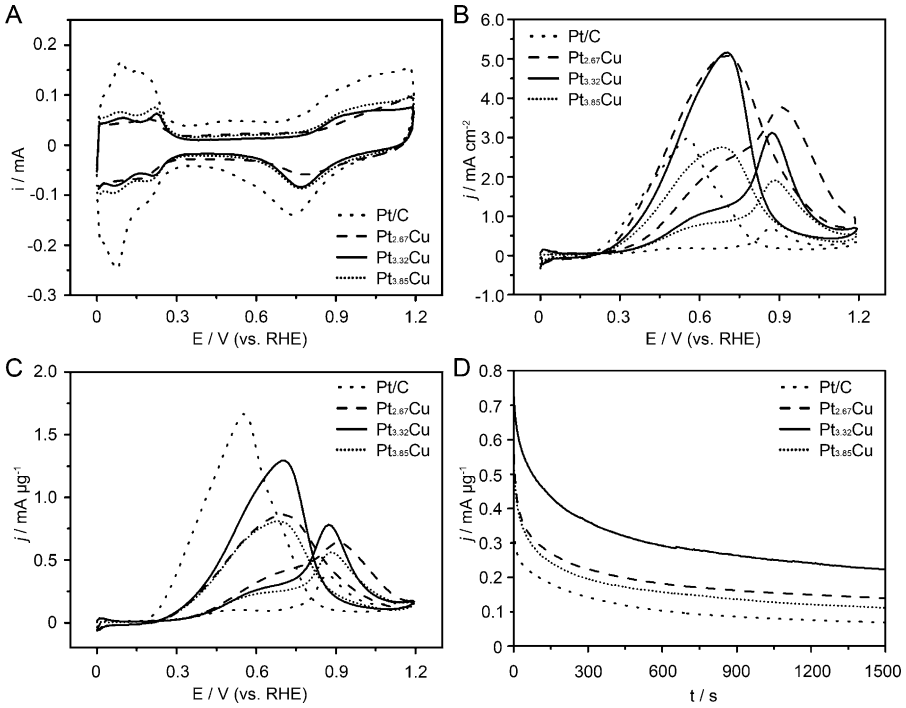

Figure 5. A) CV curves measured on three kinds of as-prepared Pt–Cu HTBNFs and commercial Pt/C in an N_2-purged solution of 0.5 M H_2SO_4 at a scan rate of 50 mV s^{-1}. B) Specific activities, C) mass activities of formic acid oxidation recorded in 0.5 M H_2SO_4 + 0.25 M HCOOH solution at a scan rate of 50 mV s^{-1}. D) Chronoamperometry curves of formic acid oxidation measured on the four catalysts in 0.5 M H_2SO_4 + 0.25 M HCOOH solution at 0.88 V. In (A), current densities were normalized in reference to the geometric area of a working electrode. Specific and mass activities are given as kinetic current densities (j) normalized in reference to the ECSAs and loading amount of Pt, respectively.

calculated as 17.0 $m^2 g^{-1}_{Pt}$ for $Pt_{2.67}Cu$, 25.1 $m^2 g^{-1}_{Pt}$ for $Pt_{3.32}Cu$, 29.6 $m^2 g^{-1}_{Pt}$ for $Pt_{3.85}Cu$ HTBNFs, and 56.0 $m^2 g^{-1}_{Pt}$ for Pt/C. Figure 5B and C exhibits the specific activities and mass activities of formic acid oxidation recorded in 0.5 M H_2SO_4 + 0.25 M HCOOH solution at a scan rate of 50 mV s^{-1}. For specific activities, the formic acid oxidation current density of $Pt_{2.67}Cu$ (3.77 mA cm^{-2}), $Pt_{3.32}Cu$ (3.12 mA cm^{-2}), and $Pt_{3.85}Cu$ (1.91 mA cm^{-2}) HTBNFs are 5.5, 4.6, and 2.8 times that of Pt/C (0.68 mA cm^{-2}), respectively. With regard to mass activities, the current density of $Pt_{2.67}Cu$ (0.64 mA g_{Pt}^{-1}), $Pt_{3.32}Cu$ (0.78 mA g_{Pt}^{-1}), $Pt_{3.85}Cu$ (0.56 mA g_{Pt}^{-1}) HTBNFs is 1.7, 2.1, and 1.5 times that of Pt/C (0.38 mA μg^{-1}), respectively, in spite of the much bigger size of HTBNFs. The reason for the improvement of the mass activities of the Pt–Cu HTBNFs with Pt/Cu ratio of 3.32 compared with those with a Pt/Cu ratio of 2.67 or 3.85 could be attributed to the synergetic effects between Pt and Cu,[4a,17] which might reach a maximum at ca. 3.32. It is clear that the as-prepared Pt–Cu HTBNFs exhibited enhanced electrocatalytic activity compared with Pt/C. In addition, the ratio of the forward peak (j_f) to the backward peak (j_b), that is, j_f/j_b, of Pt–Cu alloy HTBNFs are 0.74, 0.61, and 0.69 which are all much higher than 0.23 for Pt/C. It means that more formic acid was effectively oxidized on the Pt–Cu HTBNFs during the forward scan and less poisoning species generated during the backward scan as compared to Pt/C, which indicates a better durability.[5b,6c] The durability of Pt–Cu HTBNFs is corroborated by the chronoamperometric (CA) measurements performed at 0.88 V for 1500 s (Figure 5D). All of the HTBNFs exhibited higher specific current densities than the commercial Pt/C during the entire testing time. Additionally, for the electrocatalysts, the lower peak oxidation potential is more appropriate for fuel cells. Based on the results above, $Pt_{3.32}Cu$ HTBNFs is considered as the best electrocatalyst among the three. We conducted CV cycling in an N_2-purged 0.5 M H_2SO_4 solution from 0.6 V to 1.2 V for 1000 cycles (50 mV s^{-1}) to further test the durability of $Pt_{3.32}Cu$ HTBNFs. After 1000 cycles, the ECSAs was reduced by 19.2% for $Pt_{3.32}Cu$ HTBNFs and 33.1% for Pt/C, and the mass activity was reduced by 11.6% for $Pt_{3.32}Cu$ HTBNFs and 36.4% for Pt/C (Figure S10). Figure S10D shows that the formic acid oxidation current corresponding to the direct oxidation pathway (HCOOH→CO2) (at about 0.6 V) decreased. The result may be caused by the dealloying process of Cu to form nanocrystals with a Pt-rich surface.[5a,b,18] It was confirmed by ICP-AES measurements that the Pt/Cu ratio of Pt–Cu HTBNFS changed from 3.32 to 4.09. Even though, the j_f/j_b of Pt–Cu HTBNFs (0.64) is still much higher than 0.22 for Pt/C. Furthermore, the commercial Pt/C seemed to aggregate but Pt–Cu HTBNFs were still well preserved, as shown in Figure S11. All experimental results above demonstrate the excellent performance of Pt–Cu HTBNFs in formic acid oxidation compared to Pt/C. Considering the hierarchical structure with multiple branches, the enhanced catalytic activities are mostly ascribed to their sufficient accessible active sites at surfaces, and good electrical connection across the entire surface. Moreover, the enhanced catalytic activity is related to the possible synergetic effects between Pt and Cu.

In summary, we firstly demonstrate a facile approach to the size-controlled synthesis of ordered Pt–Cu alloy HTBNFs. In the reaction, small monopods, bipods, and tripods form at the early stage, followed by the growth of secondary, tertiary, and higher-order branches as well as the final formation of HTBNF structures. Introducing different amounts of KI into the system allows the size-controlled synthesis of HTBNFs with sizes from 110 to 250 nm. The Pt/Cu feeding ratio was found to be critical for the formation of Pt–Cu HTBNFs. Due to the unique hierarchical structure and alloy synergy, the as-prepared HTBNFs with different Pt/Cu ratios all exhibited better performance toward the oxidation of formic acid relative to commercial Pt/C. This work provides a versatile approach to the synthesis of ordered hierarchical nanoframes,

and advances our understanding of the formation of hierarchical structures.

Received: August 20, 2014
Revised: October 5, 2014
Published online: October 31, 2014

Keywords: alloys · formic acid · nanoframes · oxidation · size control

[1] a) B. C. H. Steele, A. Heinzel, *Nature* **2001**, *414*, 345 – 352; b) G. Ertl, H. Knözinger, F. Schüth, J. Weitkamp, *Handbook of Heterogeneous Catalysis*, 2nd ed., Wiley-VCH, Weinheim, **2008**, 247 – 262; c) J. Chen, B. Lim, E. P. Lee, Y. Xia, *Nano Today* **2009**, *4*, 81 – 95; d) Z. Peng, H. Yang, *Nano Today* **2009**, *4*, 143 – 164.

[2] a) A. Chen, P. Holt-Hindle, *Chem. Rev.* **2010**, *110*, 3767 – 3804; b) H. Zhang, M. Jin, Y. Xia, *Chem. Soc. Rev.* **2012**, *41*, 8035 – 8049; c) N. S. Porter, H. Wu, Z. Quan, J. Fang, *Acc. Chem. Res.* **2013**, *46*, 1867 – 1877; d) J. Wu, H. Yang, *Acc. Chem. Res.* **2013**, *46*, 1848 – 1857.

[3] a) X. Teng, M. Feygenson, Q. Wang, J. He, W. Du, A. I. Frenkel, W. Han, M. Aronson, *Nano Lett.* **2009**, *9*, 3177 – 3184; b) Y. Kang, C. B. Murray, *J. Am. Chem. Soc.* **2010**, *132*, 7568 – 7569; c) Q.-S. Chen, Z.-Y. Zhou, F. J. Vidal-Iglesias, J. Solla-Gullon, J. M. Feliu, S.-G. Sun, *J. Am. Chem. Soc.* **2011**, *133*, 12930 – 12933; d) K. Sasaki, H. Naohara, Y. Choi, Y. Cai, W. F. Chen, P. Liu, R. R. Adzic, *Nat. Commun.* **2012**, *3*, 1115; e) A.-X. Yin, X.-Q. Min, Y.-W. Zhang, C.-H. Yan, *J. Am. Chem. Soc.* **2011**, *133*, 3816 – 3819.

[4] a) X. Huang, Y. Li, Y. Li, H. Zhou, X. Duan, Y. Huang, *Nano Lett.* **2012**, *12*, 4265 – 4270; b) J. Snyder, I. McCue, K. Livi, J. Erlebacher, *J. Am. Chem. Soc.* **2012**, *134*, 8633 – 8645; c) D. Wang, H. L. Xin, R. Hovden, H. Wang, Y. Yu, D. A. Muller, F. J. DiSalvo, H. D. Abruña, *Nat. Mater.* **2013**, *12*, 81 – 87; d) S. Guo, S. Zhang, D. Su, S. Sun, *J. Am. Chem. Soc.* **2013**, *135*, 13879 – 13884; e) H. Ataee-Esfahani, M. Imura, Y. Yamauchi, *Angew. Chem. Int. Ed.* **2013**, *52*, 13611 – 13615; *Angew. Chem.* **2013**, *125*, 13856 – 13860.

[5] a) D. Xu, S. Bliznakov, Z. Liu, J. Fang, N. Dimitrov, *Angew. Chem. Int. Ed.* **2010**, *49*, 1282 – 1285; *Angew. Chem.* **2010**, *122*, 1304 – 1307; b) B. Y. Xia, H. B. Wu, X. Wang, X. W. Lou, *J. Am. Chem. Soc.* **2012**, *134*, 13934 – 13937; c) A.-X. Yin, X.-Q. Min, W. Zhu, W.-C. Liu, Y.-W. Zhang, C.-H. Yan, *Chem. Eur. J.* **2012**, *18*, 777 – 782.

[6] a) F. Saleem, Z. Zhang, B. Xu, X. Xu, X. Wang, *J. Am. Chem. Soc.* **2013**, *135*, 18304 – 18307; b) X. Liu, W. Wang, H. Li, L. Li, G. Zhou, R. Yu, D. Wang, Y. Li, *Sci. Rep.* **2013**, *3*, 1404; c) Y. Jia, Y. Jiang, J. Zhang, L. Zhang, Q. Chen, Z. Xie, L. Zheng, *J. Am. Chem. Soc.* **2014**, *136*, 3748 – 3751.

[7] a) Y. Wu, S. Cai, D. Wang, W. He, Y. Li, *J. Am. Chem. Soc.* **2012**, *134*, 8975 – 8981; b) G. Collins, M. Schmidt, C. O'Dwyer, J. D. Holmes, G. P. McGlacken, *Angew. Chem. Int. Ed.* **2014**, *53*, 4142 – 4145; *Angew. Chem.* **2014**, *126*, 4226 – 4229; c) B. T. Sneed, C.-H. Kuo, C. N. Brodsky, C.-K. Tsung, *J. Am. Chem. Soc.* **2012**, *134*, 18417 – 18426.

[8] a) M. McEachran, D. Keogh, B. Pietrobon, N. Cathcart, I. Gourevich, N. Coombs, V. Kitaev, *J. Am. Chem. Soc.* **2011**, *133*, 8066 – 8069; b) X. Hong, D. Wang, S. Cai, H. Rong, Y. Li, *J. Am. Chem. Soc.* **2012**, *134*, 18165 – 18168; c) S. Xie, N. Lu, Z. Xie, J. Wang, M. J. Kim, Y. Xia, *Angew. Chem. Int. Ed.* **2012**, *51*, 10266 – 10270; *Angew. Chem.* **2012**, *124*, 10412 – 10416; d) B. Y. Xia, H. B. Wu, X. Wang, X. W. Lou, *Angew. Chem. Int. Ed.* **2013**, *52*, 12337 – 12340; *Angew. Chem.* **2013**, *125*, 12563 – 12566; e) C. Chen, Y. Kang, Z. Huo, Z. Zhu, W. Huang, H. Xin, J. D. Snyder, D. Li, J. A. Herron, M. Mavrikakis, M. Chi, K. L. More, Y. Li, N. M. Markovic, G. A. Somorjai, P. Yang, V. R. Stamenkovic, *Science* **2014**, *343*, 1339 – 1343.

[9] a) Y. Lin, G. Yuan, R. Liu, S. Zhou, S. W. Sheehan, D. Wang, *Chem. Phys. Lett.* **2011**, *507*, 209 – 215; b) J. Zeng, Q. Zhang, J. Chen, Y. Xia, *Nano Lett.* **2010**, *10*, 30 – 35.

[10] a) B. D. Adams, G. Wu, S. Nigro, A. Chen, *J. Am. Chem. Soc.* **2009**, *131*, 6930 – 6931; b) X. Xu, J. Jia, X. Yang, S. Dong, *Langmuir* **2010**, *26*, 7627 – 7631; c) T.-H. Lin, C.-W. Lin, H.-H. Liu, J.-T. Sheu, W.-H. Hung, *Chem. Commun.* **2011**, *47*, 2044 – 2046; H.-H. Liu, J.-T. Sheu, W.-H. Hung, *Chem. Commun.* **2011**, *47*, 2044 – 2046; d) X. Chen, C.-H. Cui, Z. Guo, J.-H. Liu, X.-J. Huang, S.-H. Yu, *Small* **2011**, *7*, 858 – 863; e) Z. Wang, M. S. Bharathi, R. Hariharaputran, H. Xing, L. Tang, J. Li, Y. W. Zhang, Y. Lu, *ACS Nano* **2013**, *7*, 2258 – 2265.

[11] Note added in proof (October 9, 2014): During the preparation of our manuscript, Sun and co-workers reported the electrocatalytic activity of Pt_3Cu triangular pyramid caps: Y. Kuang, Z. Cai, Y. Zhang, D. He, X. Yan, Y. Bi, Y. Li, Z. Y. Li, X. Sun, *ACS Appl. Mater. Interfaces* **2014**, *6*, 17748 – 17752.

[12] Y.-C. Tseng, H.-S. Chen, C.-W. Liu, T.-H. Yeha, K.-W. Wang, *J. Mater. Chem. A* **2014**, *2*, 4270 – 4275.

[13] Y. Shiraishi, H. Sakamoto, Y. Sugano, S. Ichikawa, T. Hirai, *ACS Nano* **2013**, *7*, 9287 – 9297.

[14] G. Inzelt in *Encyclopedia of Electrochemistry*, *Vol. 7* (Eds.: A. J. Bard, M. Stratmann, F. Scholz, C. Pickett), Wiley-VCH, Weinheim, **2006**, pp. 43 – 44.

[15] J. Yin, J. Wang, M. Li, C. Jin, T. Zhang, *Chem. Mater.* **2012**, *24*, 2645 – 2654.

[16] a) L. Zhang, S.-I. Choi, J. Tao, H.-C. Peng, S. Xie, Y. Zhu, Z. Xie, Y. Xia, *Adv. Funct. Mater.* **2014**, DOI: 10.1002/adfm.201402350; b) M. L. Personick, M. R. Langille, J. Zhang, C. A. Mirkin, *Nano Lett.* **2011**, *11*, 3394 – 3398.

[17] J. Zhang, L. Zhang, Y. Jia, G. Chen, X. Wang, Q. Kuang, Z. Xie, L. Zheng, *Nano Res.* **2012**, *5*, 618 – 629.

[18] X. Su, D. Li, Y. Ding, W, Zhu, S. Guo, Z. Wang, S. Sun, *J. Am. Chem. Soc.* **2014**, *136*, 5745 – 5749.

